RESEARCH ARTICLE

Editor's Choice

ADVANCED FUNCTIONAL MATERIALS

www.afm-journal.de

Two-Photon Pumped Wavelength-Tunable Single-Mode Plasmonic Nanolaser with Ultralow Threshold

Long Yuan, Junfeng Lu, Meili Li,* Zhonglong Zhang, Wenjie Deng, Xiang Li, Caixia Kan, Daning Shi, Wenchao Gao,* Chunxiang Xu, and Caofeng Pan**

Nonlinear optics play an important role in laser technology, optical communication, integrated optics, and other fields. However, conventional two-photon lasing faces challenges such as high thresholds and large size, which hinder the miniaturization of lasers. In this study, the structure of single-crystal $Au/Al_2O_3/CsPbBr_3$ ($ScAu/Al_2O_3/CPB$) is constructed to achieve two-photon pumped frequency upconversion single-mode plasmonic lasing. The strong spatial confinement and near-field enhancement of surface plasmons in metals enable the plasmonic lasing mode output in a hybrid nanocavity, significantly reducing the lasing threshold. Additionally, by applying external mechanical strain, the resonant wavelength of the lasing mode is dynamically regulated, further reducing the threshold to 0.48 mJ cm^{-2} based on piezo-electronic effect. These results provide an effective strategy for all-optical integration and the development of smaller, faster, and more efficient nanophotonics devices.

1. Introduction

As an important branch of modern optics, nonlinear optics has been widely used in laser technology, optical communication, integrated optics, and other fields. Since the first experimental study of nonlinear optics, we have explored the application of different classes of materials in nonlinear optics, including bulk semiconductors, nanostructured semiconductors, and organic dyes. Following the invention of the first ruby laser by Maiman in 1960,[1] nonlinear optics based on extremely intense optical fields have been reported, such as optical harmonics,[2] optical,[3] and differential frequencies,[4] optical parametric amplification and oscillations,[5] two-photon/multiphoton absorption,[6] and so on. The most notable of these is the luminescence phenomenon induced by two-photon or multiphoton absorption, providing a new way and a platform for achieving frequency upconversion lasers.[7] However, for conventional two-photon pumped lasers, miniaturization remains a significant challenge due to the existence of optical diffraction limits.

Surface Plasmons (SP), an electromagnetic mode of photons and electrons at the interface between dielectrics and metals, provide a new way to enhance light–matter interactions at the nanoscale,[8] with the unique characteristics of highly spatial confinement and extremely near-field enhancement.[9] It can transform photon oscillation modes in conventional semiconductors into collective electron oscillation modes at metal–dielectric interfaces,[7b,10] which is not limited by the cavity size,[11] meanwhile the energy of the light field is highly localized at the interface of the metal and dielectric, breaking the diffraction limit.[12] This unique property makes surface plasmons widely used fields such as surface-enhanced Raman scattering (SERS),[13] SP resonance (SPR) biosensor,[14] and high-bandwidth plasmon photodetector.[15] They are particularly valuable in the design and construction of plasmon-coupled nanoscale lasers.[16] However, due to the existence of ohmic loss,[17] plasmonic nanolasers,[18] consisting of metal and gain medium often possesses relatively high threshold and low lasing quality.[19] Moreover, due to the limitation of two-photon absorption efficiency,[20] this nonlinear excitation behavior often requires higher incident energy density, which makes it difficult to achieve two-photon pumped plasmonic nanolasers.[21]

In this study, we prepared monocrystalline gold microsheets and synthesized $CsPbBr_3$ nanowires with excellent optical properties through the anti-solvent method, to construct a single-crystal $Au/Al_2O_3/CsPbBr_3$ ($ScAu/Al_2O_3/CPB$) hybrid nanocavity. Leveraging the low ohmic loss of single-crystal Au and the high absorption cross-section of $CsPbBr_3$ perovskite nanowire, the optical diffraction limit is broken and the single-photon pumped plasmonic nanolasers are successfully achieved. Meanwhile, by

L. Yuan, J. Lu, W. Deng, X. Li, C. Kan, D. Shi
College of Physics
Nanjing University of Aeronautics and Astronautics
Nanjing 211106, P. R. China
E-mail: lujunfeng@nuaa.edu.cn

L. Yuan, M. Li, Z. Zhang, W. Gao, C. Pan
Beijing Institute of Nanoenergy and Nanosystems
Chinese Academy of Sciences
Beijing 101400, P. R. China
E-mail: 1806386414@pku.edu.cn; gaowenchao@binn.cas.cn; pancaofeng@buaa.edu.cn

X. Li, C. Pan
Institute of Atomic Manufacturing
Beihang University
Beijing 100191, P. R. China

C. Xu
State Key Laboratory of Bioelectronics School of Biological Science and Medical Engineering
Southeast University
Nanjing 210096, P. R. China

The ORCID identification number(s) for the author(s) of this article can be found under https://doi.org/10.1002/adfm.202413250

DOI: 10.1002/adfm.202413250

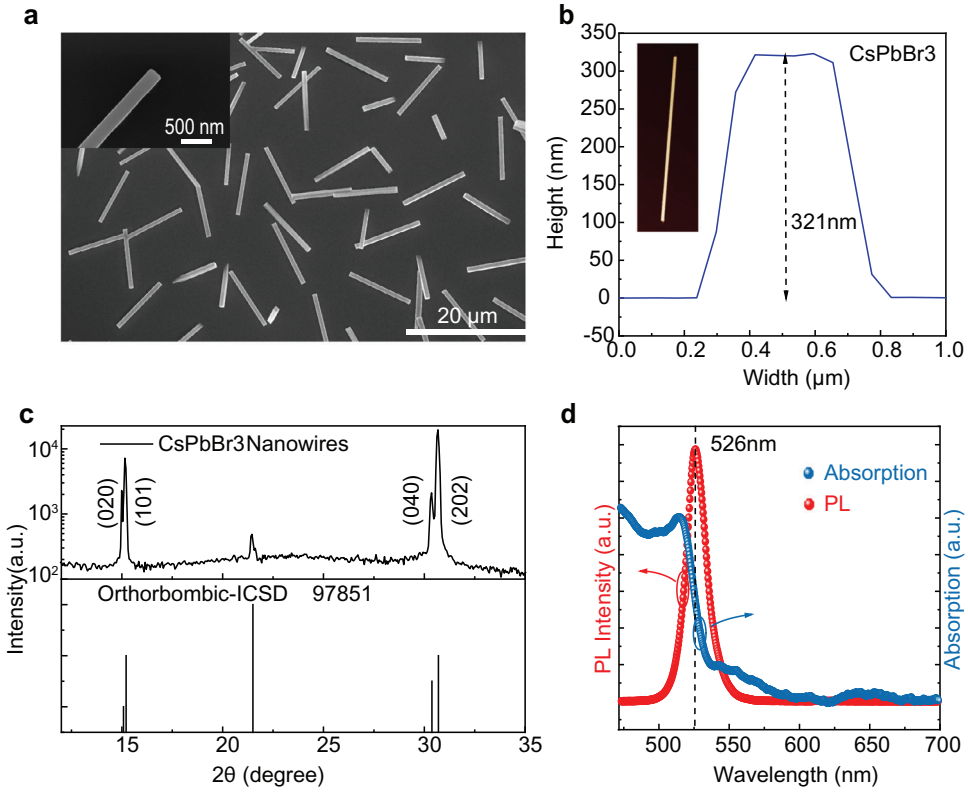

Figure 1. Morphological, structural, and optical characterization. a) SEM images of single-crystal $CsPbBr_3$ nanowires. b) The thickness of $CsPbBr_3$ nanowires as measured by atomic force microscopy (AFM). The illustration is the corresponding AFM image. c) X-ray diffraction pattern (XRD) and standard card (ICSD 97851) of orthorhombic phase $CsPbBr_3$ nanowire. d) Steady-state micro-photoluminescence (μ-PL) and absorption spectra of single $CsPbBr_3$ nanowires.

taking advantage of the extremely near-field enhancement of the surface plasmon, two-photon pumped single-mode plasmonic nanolaser with lower threshold is obtained at 800 nm femtosecond laser excitation. Finally, an external mechanical strain is applied to achieve the dynamic modulation of lasing wavelength in the range of 535.52 to 534.32 nm. Our research provides an effective solution for constructing low threshold, wavelength-tunable, frequency up-conversion plasmonic nanolasers.

2. Results and Discussion

The top view scanning electron microscope (SEM) of $CsPbBr_3$ nanowires prepared by the anti-solvent method is shown in **Figure** 1a. The magnified SEM image in the inset presents the top surface of a typical $CsPbBr_3$ nanowire, exhibiting a smooth surface and regular shape. Figure 1b shows the cross-sectional thickness of ≈321 ± 1 nm and a width of ≈500 nm for high-quality $CsPbBr_3$ nanowire, indicating that the light wave is restricted to oscillate between two parallel end faces of the structure to achieve increased amplification so that light waves can be fully confined to form a Fabry–Pérot (FP) cavity. The energy dispersive spectroscopy (EDS) mapping shows that the Cs, Pb, and Br elements are uniformly distributed in the perovskite nanowire (Figure S1, Supporting Information). The crystal structure of the perovskite nanowires was characterized by X-ray diffraction (XRD) as shown in Figure 1c, and the XRD pattern showed four distinct diffraction peaks at 14.99°, 15.15°, 30.33°, and 30.64° belong to the (020), (101), (040), and (202) crystal planes, which were in agreement with the ICSD 97851 of $CsPbBr_3$. In addition, the typical splitting of diffraction peaks ≈15° and 30° verified that the $CsPbBr_3$ nanowires prepared by the anti-solvent method belong to the orthorhombic phase structure.[22] At room-temperature, the absorption spectra and steady-state micro-photoluminescence (μ-PL) spectra of a single $CsPbBr_3$ NW on a glass substrate were measured, as shown in Figure 1d. A strong spontaneous radiation peak is observed at ≈526 nm, corresponding to the edge of the absorption band, indicating intrinsic radiative complexation between the conduction bands. The bright green fluorescence emitted by the $CsPbBr_3$ NWs (Figure S1, Supporting Information) further confirmed that it can provide sufficient gain for light amplification. All these results indicate the high-quality of the $CsPbBr_3$ NWs, which is an important factor in achieving high optical gain and exciton-surface plasmon coupling. By measuring the PL spectra at different temperatures from 80 to 300 K (Figure S2, Supporting Information), a continuous blue-shift from 525.17 to 521.79 nm and the reduced emission intensity with increasing temperature[23] for the central wavelength of PL emission peak can be observed, accompanied by a widening of the half-peak full width (FWHM). This can be attributed to the synergistic effect of thermal expansion and exciton phonon coupling in the perovskite.[24] Also, the E_b (exciton binding energy) obtained by fitting is 47 meV, which

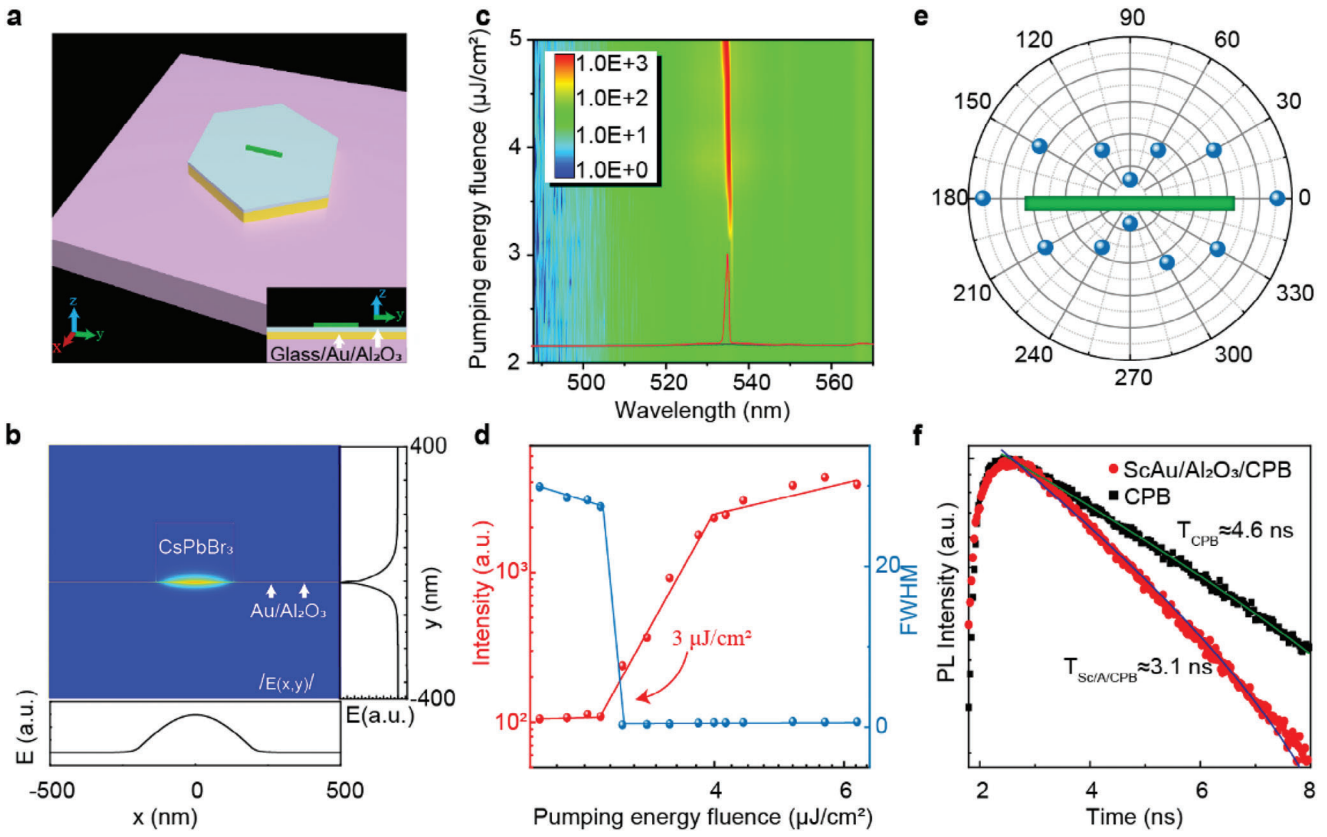

Figure 2. Single-photon pumped lasing characteristics of room-temperature plasmonic nanolaser. a) The structure diagram of ScAu/Al_2O_3/CPB device. b) The distribution of electric field (|E|) for the device at a wavelength of 534 nm calculated by the finite element method. c) 2D pseudo-color diagram of the lasing spectra of the device under the different pumping energy. d) The dependence of emission intensity and FWHM on of the pumping energy fluences. e) Polar coordinate diagram of plasmonic nanolaser emission intensity when the circular-polarized pump laser rotates the polarizer before the collection terminal. f) Time-resolved photoluminescence (TRPL) of the ScAu/Al_2O_3/CPB device and CPBNW.

is higher than the thermal ionization energy of 26 meV at room-temperature.[25] It indicates that excitons can still exist at room-temperature, which is conducive to the realization of particle population inversion and establishes a good foundation for the development of room-temperature lasers.[26]

Figure 2a shows a schematic diagram of the device structure (ScAu/Al_2O_3/CPB), where a single CPBNW is transferred onto a ScAu micron sheet (Figure S3, Supporting Information) with a 5 nm alumina (Al_2O_3) film gap layer between ScAu and CPB. The distribution of the electric-field for this device is simulated by using the finite element method, as shown in Figure 2b. It can be observed that the electric field is strongly confined to the interface between ScAu and CPBNW, presenting a very small mode volume compared to conventional F-P lasers. The lasing performance of the device (ScAu/Al_2O_3/CPB) is characterized by a femtosecond laser excitation at 390 nm. The 2D pseudo-color plots of lasing spectra under different pumping energy fluences are shown in Figure 2c. As the pumping energy fluence increases, a single narrow resonant peak appears in the SE band. When the pumping energy fluence exceeds 3 μJ cm^{-2}, the emission intensity increases sharply, accompanied by a rapid narrowing of the full width at half maximum (FWHM) as shown in Figure 2d, which demonstrates an extremely low lasing threshold of the device. The FWHM is approximately 0.29 nm, and the lasing quality factor (Q) can be estimated as ≈1850 (Figure S4, Supporting Information). Meanwhile, the lasing properties of a single $CsPbBr_3$ NWs are characterized. The lasing threshold is found to be 5.17 μJ cm^{-2} and the lasing quality factor (Q) can be estimated as ≈4146 (Figure S5, Supporting Information), indicating good optical field confinement in F-P resonators formed by single-crystal perovskite nanowires. To evaluate the polarization characteristics of the devices, the emitted light with different polarization angles from both types of devices, ScAu/Al_2O_3/CPB and bare $CsPbBr_3$ NW was collected. The different polarization behavior of light emission can be observed for the two types of devices. The former exhibits maximum intensity in the polarization direction of 0°, indicating the dominance of the transverse magnetic mode (TM),[27] while the laser intensity of the $CsPbBr_3$ NWs is maximum in the polarization direction along the 90° axis, indicating the dominance of the transverse electric mode (TE),[28] which is consistent with previous reports.[21b] Figure 2f shows the time-resolved photoluminescence (TRPL) spectra of the plasmonic device (ScAu/Al_2O_3/CPB) and $CsPbBr_3$ NW. The decay curves of ScAu/Al_2O_3/CPB and $CsPbBr_3$ NW can be fitted by a single exponential function, where the lifetimes (τ) of these two devices extracted as 3.1 and 4.6 ns, respectively. Compared to CPBNW photonic devices, the PL decay rate of the plasmonic devices is significantly increased due to the Purcell effect,

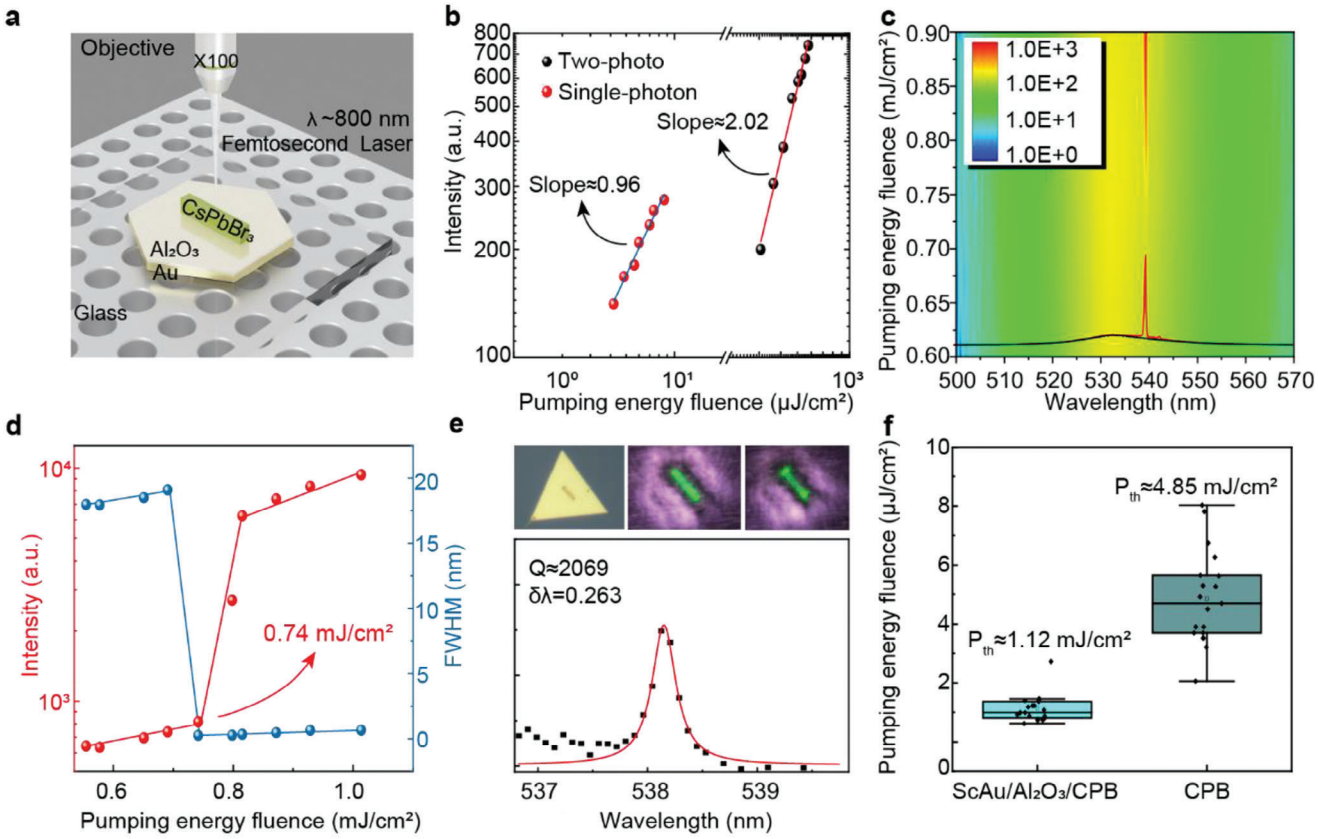

Figure 3. Two-photon pumped single-mode plasmonic nanolaser. a) Schematic diagram of the μ-PL system. b) The relationship between PL intensity and the pumping energy fluence at the excitation wavelength of 390 and 800 nm, which is fitted by power exponential function. c) 2D pseudo-color diagram of two-photon pumped single-mode lasing spectra of the plasmonic device at different pumping energy fluences. d) Dependence of the emission intensity and FWHM on pumping energy fluence. e) Enlarged image of the laser threshold mode fitted by the Lorentz function, illustrated as the optical image of the two-photon pumping of the plasmonic nanolaser at $p > p_{th}$ and $p < p_{th}$. f) Comparison of threshold values between ScAu/Al_2O_3/CPB plasmonic devices and bare $CsPbBr_3$ nanowires.

implying effective coupling between SPs of Au and excitons of CPB.

In order to study the nonlinear optical behavior of the plasmonic device (ScAu/Al_2O_3/CPB), the two-photon pumped lasing spectra of ScAu/Al_2O_3/CPB hybrid nanocavity were measured using femtosecond laser excitation at a wavelength of 800 nm through the same μ-PL system as shown in **Figure** 3a. Figure 3b compares the dependence of PL intensity on the effect of pump energy fluence for single-photon and two-photon excitations at 390 and 800 nm wavelengths, which can be fitted as a power exponential function of $I \propto p^{\gamma}$. Under the excitation wavelength of 390 and 800 nm femtosecond laser, the power-law exponents of γ can be extracted as ≈0.96 and ≈2.02, respectively.[29] The relationship between PL intensity and pumping energy fluence of the former is approximately linear, indicating that single-photon excitation is dominant. The latter shows a quadratic power dependence, indicating that two photons participate in the absorption process due to the low energy of the excitation photon. Figure 3c shows the two-photon pumped lasing spectra of the plasmonic device excited by a 800 nm femtosecond. With increasing of the pumping energy fluences, an extremely narrowing resonant peak with a FWHM of≈0.263 nm and Q factor of ≈2069 appears, as shown in Figure 3e, indicating a transition from spontaneous emission to stimulated emission. The dependence of pumping energy fluence on emission intensity is shown in Figure 3d. It can be observed that the threshold of the plasmonic device excited by two-photon is ≈0.74 mJ cm^{-2}, which is two orders of magnitude larger than that of single-photon pumped device. It indicates that the efficiency of two-photon excitation is much lower than that of single-photon excitation. In order to further understand the lasing characteristics, the lasing spectra of the plasmonic devices with different cavity lengths from 5.47 to 7.49 μm were measured (Figure S6a, Supporting Information). It can be observed that the number of resonant modes in the gain region decreases with reduction in hybrid nanocavity size. As the cavity size reduces to ≈5.47 μm, the single-mode lasing output is formed due to the existence of self-absorption effect in gain medium and the giant "Frequency Pulling" effect in plasmonic device (Figure S6b, Supporting Information).[30]

Interestingly, the lasing threshold of the photonic devices is significantly higher than that of the plasmonic devices under the two-photon pumped conditions. Two-photon pumped lasing properties of the individual $CsPbBr_3$ NW was also characterized. The lasing threshold was found to be 5.30 mJ cm^{-2} and the Q factor can be estimated as ≈2561 (Figure S8, Supporting Information), whose lasing threshold is nearly an order of

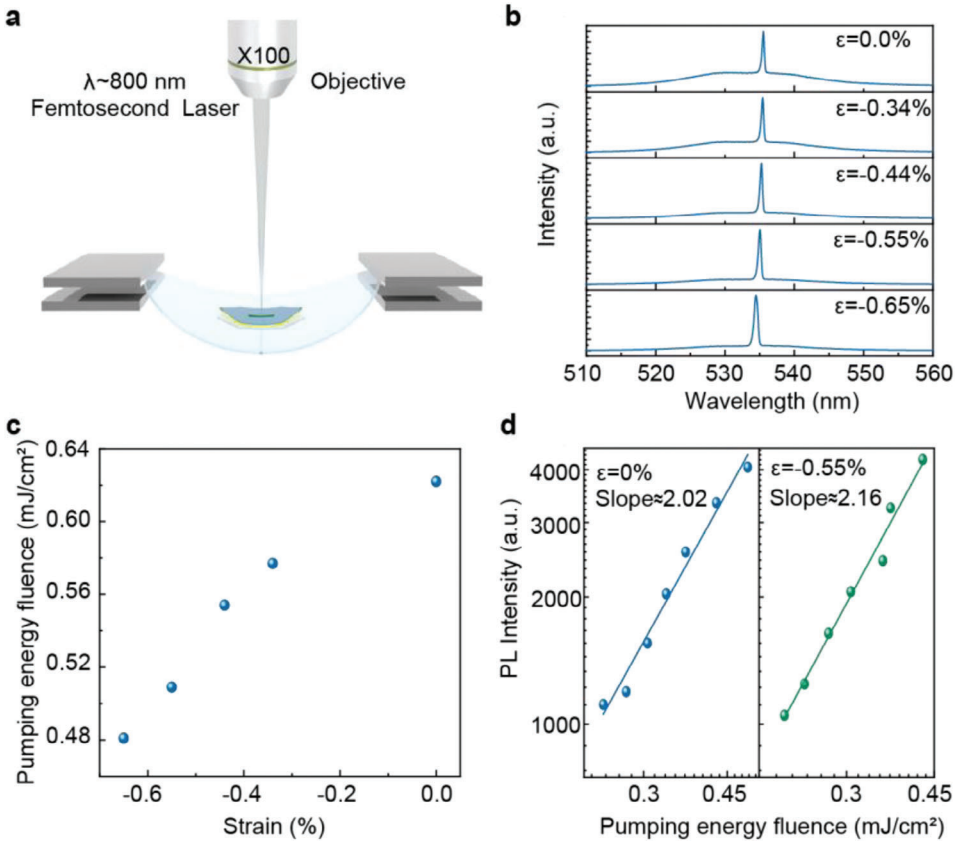

Figure 4. Dynamic regulation of lasing wavelength of ScAu/Al_2O_3/CPB plasmonic device under compressive strain (ϵ). a) Schematic diagram of plasmonic device pumped by femtosecond laser under compressive stress. b) Spectra of same plasmonic device with different compressive strain from 0% to −0.65%. c) Change of threshold value with compressive strain. d) The dependence of PL intensity pumping energy fluences at ϵ = 0% and −0.55%.

magnitude larger than that of the plasmonic devices. To clarify the physical mechanisms involved, a new device structure where a single CPBNW is partially on a ScAu/Al_2O_3 substrate and partially on a SiO_2 substrate using fixed-point transfer (Figure S7a, Supporting Information). The comparison of the PL intensities of the plasmonic and photon parts under 800 nm femtosecond lasing excitation at the same pumping energy fluence is shown in Figure S7b (Supporting Information). The PL intensity of the plasmonic part is higher than that of the photon part under the same pumping energy fluence. The PL intensity of the plasmonic structure increases more rapidly with increasing pumping energy fluence and is higher than that of the photonic structure (Figure S7c, Supporting Information), indicating an increased proportion of exciton recombination. The higher PL intensity indicates that the introduction of Au surface plasmons results in an increase in exciton coupling efficiency due to its near-field enhancement effect, which increases the optical gain and promotes a decrease in the lasing threshold. To verify this interesting phenomenon, 19 plasmonic devices, and 19 photonic devices were selected for lasing threshold comparison under two-photon pumping conditions. It can be observed that the lasing threshold of plasmonic devices is much lower than that of photonic devices shown in Figure 3f. By means of average calculation, the lasing threshold of the latter is nearly five times higher than that of the former. These experimental results demonstrate the universality of the low-threshold characteristics of the plasmonic devices, mainly attributed to the resonant coupling between the pump-photo-excited gold-surface plasmonic excitons and the CPB excitons, which effectively enhances the exciton complex efficiency. This is an important manifestation of the extreme near-field enhancement property of metal surface plasmonic excitons.

Moreover, we transferred ScAu micrometer sheets to a flexible PEN substrate and constructed plasmonic devices on the flexible substrate, achieving wavelength-tunable two-photon pumped plasmonic nanolaser based on strain engineering. **Figure** 4a shows a plasmonic device excited with a femtosecond laser at 800 nm using the same μ-PL system, with an external mechanical strain applied to the substrate. The two-photon pumped plasmonic lasing wavelength is continuously blue-shifted from 535.52 to 534.32 nm, as shown in Figure 4b. It can be attributed to the external mechanical strain-induced change in the effective refractive index of the hybrid nanocavity, the value of which is jointly determined by the dielectric constant of both the gain medium and the metal. Interestingly, the lasing peak intensity gradually increases with the gradual increase of external mechanical compressive strain (Figure S9b, Supporting Information). It can be attributed to the fact that the application of external mechanical strain makes the resonant energy of surface plasmons and the excitonic energy more compatible, which promotes the exciton complex efficiency.[31] And the effective improvement of

the optical gain provides an important prerequisite for further reduction of the lasing threshold. With the increase of compressive strain, the threshold of the plasmonic device (ScAu/Al_2O_3/CPB) reduced from 0.62 to 0.48 mJ cm^{-2}, with a performance improvement of 23%, as shown in Figure 4c. The results for the threshold of the device (ScAu/Al_2O_3/CPB) compared to previously reported results for other plasmonic lasers are summarized in Table S1 (Supporting Information), which is the lowest value reported in the literature. It provides an effective strategy to further reduce the plasmonic excitation lasing threshold for two-photon pumping. Figure 4d shows the relationship between the PL intensity and pumping energy fluence at compressive strains of 0% and −0.55%. With the increase of compressive strain, the power-law exponent increases slightly but still maintains a nearly quadratic growth, indicating that the TPA plays an important role in the excitation process, which directly reflects the nonlinear optical properties of CPBNW.[32] As mentioned above, due to the external perturbation, the positive and negative charges inside the crystal are separated and a dipole moment is generated to change the polarization, which effectively modulates the refractive index and nonlinear absorption of the material, providing a new idea for lowering the threshold and dynamically modulating the nonlinear optical response.

3. Conclusion

In summary, under the excitation of 800 nm femtosecond laser, a high-quality two-photon pumped single-mode plasmonic lasing output is achieved in a hybrid Au/Al_2O_3/$CsPbBr_3$ (ScAu/Al_2O_3/CPB) plasmonic device structure with a threshold of 0.74 mJ cm^{-2} and Q factor of 2069. By designing a flexible plasmonic nanolaser with the PEN/single-crystal-Au/Al_2O_3/$CsPbBr_3$ structure, the threshold is effectively reduced from 0.62 to 0.48 mJ cm^{-2} under the excitation of 800 nm femtosecond laser through strain engineering. The continuous blue shift of lasing wavelength from 535.52 to 534.32 nm is also realized, which can be attributed to the change in the effective refractive index of the hybrid nanocavity induced by the piezoelectric polarization effect. Our work introduces a new way to improve the lasing performance of piezoelectric semiconductor materials and will expand the application of piezoelectric effects in flexible lasers and on-chip strain sensing.

4. Experimental Section

Preparation of $CsPbBr_3$ Perovskite Single-Crystal Nanowires: The $CsPbBr_3$ precursor solution was prepared by dissolving CsBr and $PbBr_2$ powder (Alfa Aesar, 99.999%) in anhydrous dimethylformamide (DMF) with a molar ratio. The concentration of the $CsPbBr_3$ precursor solution was maintained at 0.01 M. This prepared precursor solution was stirred at 45 °C for 24 h and filtered for use. Subsequently, $CsPbBr_3$ nanowires were prepared via the anti-solvent method using toluene as the anti-solvent. The $CsPbBr_3$ precursor solution (≈30 µL) was dropped onto a slide (18 mm × 18 mm) and placed in a small dish within a larger dish. A certain amount of toluene (≈30 µL) was added into a larger petri dish as an anti-solvent, and 3 M Parafilm with small holes was used to seal it to control the volatilizing rate of the $CsPbBr_3$ precursor solution under the action of toluene vapor. Finally, $CsPbBr_3$ nanowires were grown in an oven at 30 °C. The length and diameter of different nanowires were controlled by adjusting the growth rate of the $CsPbBr_3$ precursor fluid through the volatilization rate.

Preparation of 2D Single-Crystal Gold Microsheets: The precursor was prepared by adding 333 mg polyvinylpyrrolidone (PVP) into 1.5 mL of glycol solution, stirring until completely dissolved. Subsequently, 7 mL of glycol solution was heated to 150 °C (ethylene glycol boiling point is 198 °C). Next, 0.1 mL of tetrachloroauric acid ($HAuCl_4 \bullet 3H_2O$, 50% Au basis, Sigma, 99.99%) was added to the ethylene glycol solution, with temperature controlled at 140 °C, the mixture was stirred for 15 min. Then, the solution was placed in a blast fume hood, with the reaction temperature controlled at 140 °C. The prepared precursor solution was added drop by drop until the entire solution was used. The reaction was allowed to proceed until the solution turned gold and transparent. After cooling, the solvent was changed to isopropyl alcohol for further use.

Fabrication of Plasmonic Device: The prepared gold microsheet was transferred to the glass substrate by using the drip method, and the 5 nm Al_2O_3 film was deposited on the surface of the gold micro sheet using an ALD atomic layer deposition system. Subsequently, the $CsPbBr_3$ nanowires grown using the anti-solvent method were transferred to the surface of the gold micro sheet using a 2D material positioning transfer system. This process resulted in the preparation of a plasmonic nanolaser with the ScAu/Al_2O_3/$CsPbBr_3$ NWs structure.

Morphology and Structural Characterization: Scanning electron microscopy (SEM, SU8020, Hitachi), X-ray diffraction (XRD, D/MAX-2400, Rigaku, Cu Kα radiation), and atomic force microscopy (AFM, Cypher S, Asylum Research) were used to morphologically and structurally characterize the as-prepared $CsPbBr_3$ nanowires, and single-crystalline Au microsheets.

Numerical Calculations: The finite-element method (COMSOL) was used for numerical calculations. By placing the $CsPbBr_3$ nanowire on the Al_2O_3/Au substrate, the effective index (n_{eff}) and propagation distance (L_m) of the $CsPbBr_3$ nanowire with the thickness (T) of the $CsPbBr_3$ nanowire were calculated. The refractive index of $CsPbBr_3$ and Al_2O_3 at λ = 534 nm were 2.19, and 1.768,[33] respectively, during the simulations. The Au films were described by the Drude model based on Johnson's experiments.[34] A full 3D simulation was performed using a hybrid plasmonic mode as input, and the near-field electric field distribution and far-field emission were calculated.

Supporting Information

Supporting Information is available from the Wiley Online Library or from the author.

Acknowledgements

The authors thank the support of the Fundamental Research Funds for the Central Universities (No. NS2024063), National Natural Science Foundation of China (No. 61805015, 62105035, 52125205, 52250398, U20A20166, 12374257, 52192614 and 52003101), the Natural Science Foundation of Jiangsu Province (BK20231441) and the Nanjing University of Aeronautics and Astronautics Graduate Student Research and Practice Innovation Program (xcxjh20232108, xcxjh20232101), National key R&D program of China (2021YFB3200300), Natural Science Foundation of Beijing Municipality (2222088), Shenzhen Science and Technology Program (Grant No. KQTD20170810105439418) and the Fundamental Research Funds for the Central Universities.

Conflict of Interest

The authors declare no conflict of interest.

Data Availability Statement

The data that support the findings of this study are available from the corresponding author upon reasonable request.

Keywords

low-threshold, mode regulation, plasmonic nanolaser, single-mode, two-photon pumping

Received: July 24, 2024
Revised: September 22, 2024
Published online:

[1] T. H. Maiman, *Nature* **1960**, *187*, 493.
[2] R. W. Terhune, P. D. Maker, C. M. Savage, *Phys. Rev. Lett.* **1962**, *8*, 404.
[3] J. A. Armstrong, N. Bloembergen, J. Ducuing, P. S. Pershan, *Phys. Rev.* **1962**, *127*, 1918.
[4] N. M. Kroll, *Phys. Rev.* **1962**, *127*, 1207.
[5] W. Kaiser, C. G. B. Garrett, *Phys. Rev. Lett.* **1961**, *7*, 229.
[6] P. A. Franken, J. F. Ward, *Rev. Mod. Phys.* **1963**, *35*, 23.
[7] a) R. R. Bao, C. F. Pan, *Sci. Bull.* **2022**, *67*, 2263; b) S. P. Ge, L. B. Huang, C. F. Pan, *Sci. Bull.* **2022**, *67*, 1018.
[8] J. F. Lu, C. X. Xu, F. T. Li, Z. Yang, Y. Y. Peng, X. Y. Li, M. L. Que, C. F. Pan, Z. L. Wang, *ACS Nano* **2018**, *12*, 11899.
[9] S. A. Maier, P. G. Kik, H. A. Atwater, S. Meltzer, E. Harel, B. E. Koel, A. A. G. Requicha, *Nat. Mater.* **2003**, *2*, 229.
[10] Q. Zhang, S. L. Zuo, P. Chen, C. F. Pan, *InfoMat* **2021**, *3*, 987.
[11] a) Y. H. Wu, L. B. Huang, C. F. Pan, *Sci. Bull.* **2023**, *68*, 1849; b) J. L. Sun, T. S. Li, L. Dong, Q. L. Hua, S. Chang, H. Z. Zhong, L. J. Zhang, C. X. Shan, C. F. Pan, *Sci. Bull.* **2022**, *67*, 1755.
[12] a) Y. Wang, J. Yu, Y. F. Mao, J. Chen, S. Wang, H. Z. Chen, Y. Zhang, S. Y. Wang, X. Chen, T. Li, L. Zhou, R. M. Ma, S. Zhu, W. Cai, J. Zhu, *Nature* **2020**, *581*, 401; b) J. Wang, X. H. Jia, Z. T. Wang, W. L. Liu, X. J. Zhu, Z. T. Huang, H. C. Yu, Q. X. Yang, Y. Sun, Z. J. Wang, S. C. Qu, J. Lin, P. Jin, Z. G. Wang, *Nanoscale* **2020**, *12*, 16403.
[13] a) Y. Liang, C. Li, Y. Z. Huang, Q. Zhang, *ACS Nano* **2020**, *14*, 14375; b) S. Cho, Y. Yang, M. Soljačić, S. H. Yun, *Sci. Adv.* **2021**, *7*, eabf3362.
[14] a) N. C. Lindquist, C. D. L. de Albuquerque, R. G. Sobral-Filho, I. Paci, A. G. Brolo, *Nat. Nanotechnol.* **2019**, *14*, 981; b) R. Pilot, R. Signorini, C. Durante, L. Orian, M. Bhamidipati, L. Fabris, *Biosensors* **2019**, *9*, 57.
[15] J. Langer, D. Jimenez de Aberasturi, J. Aizpurua, R. A. Alvarez-Puebla, B. Auguié, J. J. Baumberg, G. C. Bazan, S. E. J. Bell, A. Boisen, A. G. Brolo, J. Choo, D. Cialla-May, V. Deckert, L. Fabris, K. Faulds, F. J. García de Abajo, R. Goodacre, D. Graham, A. J. Haes, C. L. Haynes, C. Huck, T. Itoh, M. Käll, J. Kneipp, N. A. Kotov, H. Kuang, E. C. Le Ru, H. K. Lee, J. F. Li, X. Y. Ling, et al., *ACS Nano* **2020**, *14*, 28.
[16] M. Piliarik, M. Vala, I. Tichý, J. Homola, *Biosens. Bioelectron* **2009**, *24*, 3430.
[17] Y. Zhao, M. Lei, S. X. Liu, Q. Zhao, *Sens. Actuators B Chem* **2018**, *261*, 226.
[18] C. Hoessbacher, A. Josten, B. Baeuerle, Y. Fedoryshyn, H. Hettrich, Y. Salamin, W. Heni, C. Haffner, C. Kaiser, R. Schmid, D. L. Elder, D. Hillerkuss, M. Möller, L. R. Dalton, J. Leuthold, *Opt. Express* **2017**, *25*, 1762.
[19] a) Z. Yang, J. F. Lu, M. H. ZhuGe, Y. Cheng, J. F. Hu, F. T. Li, S. Qiao, Y. F. Zhang, G. F. Hu, Q. Yang, D. F. Peng, K. H. Liu, C. F. Pan, *Adv. Mater.* **2019**, *31*, 10; b) Y. Liu, J. Tao, Y. P. Mo, R. R. Bao, C. F. Pan, *Adv. Mater.* **2024**, *36*, 2313857.
[20] R. M. Ma, R. F. Oulton, V. J. Sorger, G. Bartal, X. A. Zhang, *Nat. Mater.* **2011**, *10*, 110.
[21] a) R. M. Ma, R. F. Oulton, *Nat. Nanotechnol* **2019**, *14*, 12; b) Z. T. Huang, J. W. Chen, H. Li, Y. Z. Zhu, Q. N. Cui, C. X. Xu, T. C. Lu, *Adv. Opt. Mater.* **2022**, *10*, 7.
[22] R. Bao, J. Tao, J. Zhao, M. Dong, J. Li, C. Pan, *Sci. Bull.* **2023**, *68*, 1027.
[23] M. J. Crane, L. M. Jacoby, T. A. Cohen, Y. Huang, C. K. Luscombe, D. R. Gamelin, *Nano Lett.* **2020**, *20*, 8626.
[24] S. H. Yu, J. Xu, X. Y. Shang, E. Ma, F. L. Lin, W. Zheng, D. T. Tu, R. F. Li, X. Y. Chen, *Adv. Sci.* **2021**, *8*, 12.
[25] J. Tao, M. Dong, L. Li, C. Wang, J. Li, Y. Liu, R. Bao, C. Pan, *Microsyst. Nanoeng.* **2020**, *6*, 62.
[26] R. H. Han, Y. Liu, Y. P. Mo, H. C. Xu, Z. W. Yang, R. R. Bao, C. F. Pan, *Adv. Funct. Mater.* **2023**, *33*, 2305531.
[27] G. C. Wu, X. Li, R. R. Bao, C. F. Pan, *Adv. Funct. Mater.* **2024**, https://doi.org/10.1002/adfm.202405722.
[28] Z. Y. Chen, R. H. Zhou, J. Y. Huang, H. C. Xu, Z. M. Li, Y. S. Wang, R. R. Bao, J. He, C. F. Pan, *Adv. Funct. Mater.* **2024**, https://doi.org/10.1002/adfm.202406434.
[29] J. F. Lu, X. P. He, J. Xu, F. T. Li, Q. B. Tang, X. X. Wang, J. Dai, Q. S. Yao, F. F. Qin, C. X. Xu, *Adv. Funct. Mater.* **2024**, *34*, 7.
[30] a) R. F. Oulton, V. J. Sorger, T. Zentgraf, R. M. Ma, C. Gladden, L. Dai, G. Bartal, X. Zhang, *Nature* **2009**, *461*, 629; b) J. F. Lu, C. Y. Zhang, F. T. Li, R. Wang, F. F. Qin, G. Y. Zhu, *Appl. Phys. Lett.* **2022**, *120*, 6.
[31] M. L. Li, J. F. Lu, P. Wan, M. M. Jiang, F. Lin, X. X. Wu, X. F. Liu, C. F. Pan, *Adv. Opt. Mater.* **2023**, *11*, 8.
[32] J. F. Lu, F. T. Li, W. D. Ma, J. F. Hu, Y. Y. Peng, Z. Yang, Q. S. Chen, C. X. Xu, C. F. Pan, Z. L. Wang, *Adv. Sci.* **2019**, *6*, 8.
[33] L. Y. Chen, D. W. Lynch, *Phys. Rev. B* **1987**, *36*, 1425.
[34] S. J. Youn, T. H. Rho, B. I. Min, K. S. Kim, *PSS B-Bas. Solid State Phys.* **2007**, *244*, 1354.

